# Nanoscale Mapping of the Directional Flow Patterns at Liquid-Solid Interfaces

Luca Piantanida [1,‡] Amir F. Payam [1,§] Jing Zhong,[2,†] and Kislon Voïtchovsky [1,*]

[1] *Department of Physics, Durham University, Durham, United Kingdom*
[2] *School of Civil Engineering, Harbin Institute of Technology, Harbin, China*

The nanoscale behavior of liquid molecules and solutes along the interface with solids controls many processes such as molecular exchanges, wetting, electrochemistry, nanofluidics, biomolecular function, and lubrication. Experimentally, several techniques can explore the equilibrium molecular arrangement of liquids near the surface of immersed solids but quantifying the nanoscale flow patterns naturally adopted by this interfacial liquid remains a considerable challenge. Here we describe an approach based on atomic force microscopy, and able to quantify the flow direction preferentially adopted by liquids along interfaces with nanoscale precision. The approach, called vortex dissipation microscopy (VDM), uses high-frequency directional oscillations to derive local flow information around each location of the interface probed. VDM effectively derives nanoscale flow charts of the interfacial liquid parallel to a solid and can operate over a broad range of soft and hard interfaces. To illustrate its capabilities, we quantify the dynamics of aqueous solutions containing KCl or $MgCl_2$ along the surface of a same graphene oxide flake. We show that dissolved $K^+$ ions can move evenly in all directions along the interface whereas $Mg^{2+}$ ions tend to move in registry with the underlying lattice due to enthalpic effects. The results provide *in situ* nanoscale insights into the ion-specific sieving properties of graphene oxide membranes.

## I. INTRODUCTION

In bulk liquids molecules diffuse randomly in all directions unless an external perturbation is imposed; no long-range molecular order is present. This picture breaks down when liquid molecules meet a wall. At the interface with immersed solids, liquid molecules and dissolved solutes tend to move more slowly and often adopt a more ordered arrangement compared to when in the bulk [1–3]. This is due to a loss of configurational entropy and the molecules interacting with the solid's surface. This so-called interfacial liquid is ubiquitous in nature and in technology where it underpins numerous phenomena. Examples include protein function [4,5], molecular diffusion at interfaces during self-assembly [6], the functionalization of surfaces [7], wetting [8], lubrication [9], nanofluidics [10], electrochemistry and heterogeneous catalysis [11], and the functioning of energy cells [12] to name but a few.

Understanding the properties and behavior of interfacial liquid is therefore of paramount importance to scientists and technologists alike. The task is however challenging because the interfacial liquid typically spans only a few molecular layers (approximately <2 nm) near the surface of the solid. On regular interfaces such as single crystals, the most accurate measurements typically rely on averaging over a large number of interfacial molecules to increase the signal-to-noise ratio of measurements [3]. Averaging approaches can be problematic for irregular interfaces or systems where local contextual information is important. This is the case for many biological and electrochemical systems where the efficiency of interfacial processes hinge on particular nanoscale topographic or chemical features at a given location of the solid's surface. These difficulties can, in principle, be overcome by using local techniques such as atomic force microscopy (AFM) where a nanoscale probe is used to explore the interface. Recent advances in the field of AFM have enabled significant improvement in the technique with subnanometer spatial resolution being now routine [13–15], three-dimensional mapping of the liquid density in the vicinity of the solid [16,17],

---

*kislon.voitchovsky@durham.ac.uk
†zhongjing@hit.edu.cn
‡Present address: Micron School of Materials Science & Engineering, Boise State University, Boise, USA. lucapiantanida@boisestate.edu
§Present address: School of Engineering, Ulster University, Belfast, United Kingdom. a.farokh-payam@ulster.ac.uk

high-accuracy mapping of the interfacial rheology and the viscoelastic properties of soft biological samples [18,19], and high-speed measurements [20–22].

While these developments have enabled new research, it is usually the unperturbed equilibrium molecular arrangement of the interfacial liquid that is being probed. No information about the local liquid dynamics or natural convective flows are available on that scale. This is a serious limitation of the technique because interfacial processes are dynamical in essence and often rely on the flow motion of liquid molecules near the solid's surface to proceed.

One possible way forward is to exploit the fact that AFM physically probes the interface with a moving nanoscale tip. As the tip moves across or through the interfaces and pushes the liquid molecules, it experiences a resistance related to the ability of the molecules to flow along the solid's surface [23]. Physically, this is quantified by the so-called slip length of the liquid at the interface, the distance beneath the solid's surface where the lateral velocity component of the liquid molecules would vanish, based on the extrapolated flow profile [24,25]. In aqueous solutions, the energy needed to displace the liquid molecules located immediately under the tip is directly related to the local slip length [23], itself determined by the local affinity of the liquid for the solid [26]. This relationship quantitatively links the ability of liquid molecules to flow along the interface with the measurable energy needed to move the tip through the interface, therefore offering an opportunity to quantify nanoscale interfacial flow patterns. Practically, this entails the ability for the tip to probe all the possible flow directions around a given location and accurately quantify the energy dissipation associated with each direction. This task is currently not possible with existing AFM systems.

In this study we develop an approach to derive directional and quantitative information about the ability of liquids to flow laterally at solid-liquid interfaces with nanometer resolution. The method, based on a commercial AFM augmented with ultrafast nanoactuators, effectively maps the local flow patterns naturally occurring at the interface, similarly to the maps of maritime currents in navigation. In order to illustrate the method's capability, we use it to investigate the flow of aqueous solutions containing potassium chloride (KCl) and magnesium chloride ($MgCl_2$) at the interface with sheets of graphene oxide (GO). The two types of cations ($K^+$ and $Mg^{2+}$) are well known to behave very differently when sieved through membranes composed of stacked GO sheets [27,28]. Water molecules can easily permeate through the membrane but cation-specific permeation has been reported [29,30], explained by differences in the ions' hydration structures when moving at the interface with GO [31]. Mapping the flow patterns forming at the surface of GO in the presence of each type of salt provides molecular-level insights into the molecular mechanisms enabling ion-specific sieving by GO membranes.

## II. METHODS

### A. Sample preparation

The imaging solutions are made using ultrapure water (18.2 MΩ, Merck-Millipore, Watford, UK) and chemicals purchased from Sigma Aldrich (Gillingham, UK) and used without further purification.

Grade V mica, purchased from SPI supplies (West Chester, PA, USA), is freshly cleaved before adding a drop (100 μl) of solution and starting the experiment immediately after.

Bovine lens membranes are purified and deposited onto freshly cleaved mica following a protocol described elsewhere in detail [32]. In short, 10 μl of lens membrane fragments are dissolved in a 30 μl solution composed of 25 mM $MgCl_2$, 150 mM KCl, and 10 mM Tris at pH 7.4. The resulting solution is deposited onto freshly cleaved mica and incubated for 15 min. Subsequently, the sample is rinsed gently six times with a solution containing 150 mM KCl and 10 mM Tris at pH 7.4 to remove loosely attached membrane fragments. More solution is then added to conduct the experiment.

GO is prepared from natural graphite (SigmaAldrich, <45 μm) flakes by a modified Hummers' method as described in Refs. [33,34]. As-prepared GO being in gel state, it is subjected to thorough dialysis against ultrapure water to completely remove residual salts and acids. This resulted in a 10 mg/ml aqueous dispersion of GO flakes in ultrapure water. The surface of GO is highly charged in aqueous solutions, mainly due to its carboxyl, hydroxyl and alkoxyl groups, which ensure its perfect dispersion. Near neutral pH and in conditions close to the present study, zeta potential measurements reveal a negatively charged surface with values close to −30 mV [35–37]. For the experiments, the GO dispersion is diluted ten times in 10 mM KCl reaching a final concentration of 1 mg/ml. A droplet (50 μl) of this dispersion is placed on top of a freshly cleaved HOPG (SPI supplies) and incubated for 40 min at room temperature. The sample is then slowly rinsed six times with more 10 mM KCl solution to remove loosely adsorbed GO flakes and prevent the deposition of flakes on the AFM cantilever. More clean solution is then added to conduct the experiment.

### B. AFM and VDM imaging

All experiments are conducted on a commercial Cypher ES AFM (Asylum Research, Oxford Instruments, Santa Barbara, CA, USA) with the tip and cantilever fully immersed into the liquid. The vertical oscillation of the tip is controlled by photothermal excitation (Blue Drive) and the experiments are conducted at 25.0 ± 0.1°C (controlled). Before imaging a small droplet of the desired solution is used to prewet the AFM cantilever and holder so as to avoid the formation of air bubbles. All experiments

are conducted with the feedback on the tip oscillation amplitude (amplitude-modulation mode). The imaging setpoint is optimized for VDM, typically requiring lower setpoint values than for standard AFM [38]. In order to allow for direct comparability between measurements on GO, the experiments are carried out in 10 mM KCl and 10 mM $MgCl_2$ over an identical location (same GO flake), with the same tip and same imaging conditions. To avoid possible cross-contamination, the experiment is first conducted in KCl and subsequently in $MgCl_2$, using extensive rinsing in between.

## III. RESULTS

### A. The vortex dissipation microscope

The basic principles of the microscope developed here are presented in Fig. 1. The idea is to combine the high-resolution imaging capabilities of dynamic mode AFM—a

vertically vibrating tip at a set interface location—with the directional information available from shear force microscopy measurements—a laterally moving tip at a set distance from the solid. When operated with amplitudes comparable to the size of the interface (typically <1–2 nm), both approaches have been shown to probe local liquid slippage at the interface [14,23]. In the former, the liquid molecules are pushed indiscriminately as the tip squeezes out the interfacial liquid [14], while in the latter the direction of motion of the liquid molecules is defined, but at the cost of lateral resolution [23].

In order to retain the high-resolution capabilities of dynamic mode AFM while simultaneously gaining the directional insights from shear force microscopy, a combined vertical and lateral oscillatory motion is applied to the tip. Practically, this is achieved by operating the AFM in a standard dynamic mode (here amplitude modulation with a tip vertical-oscillation frequency $\nu_{\text{tip}}$) and impos-
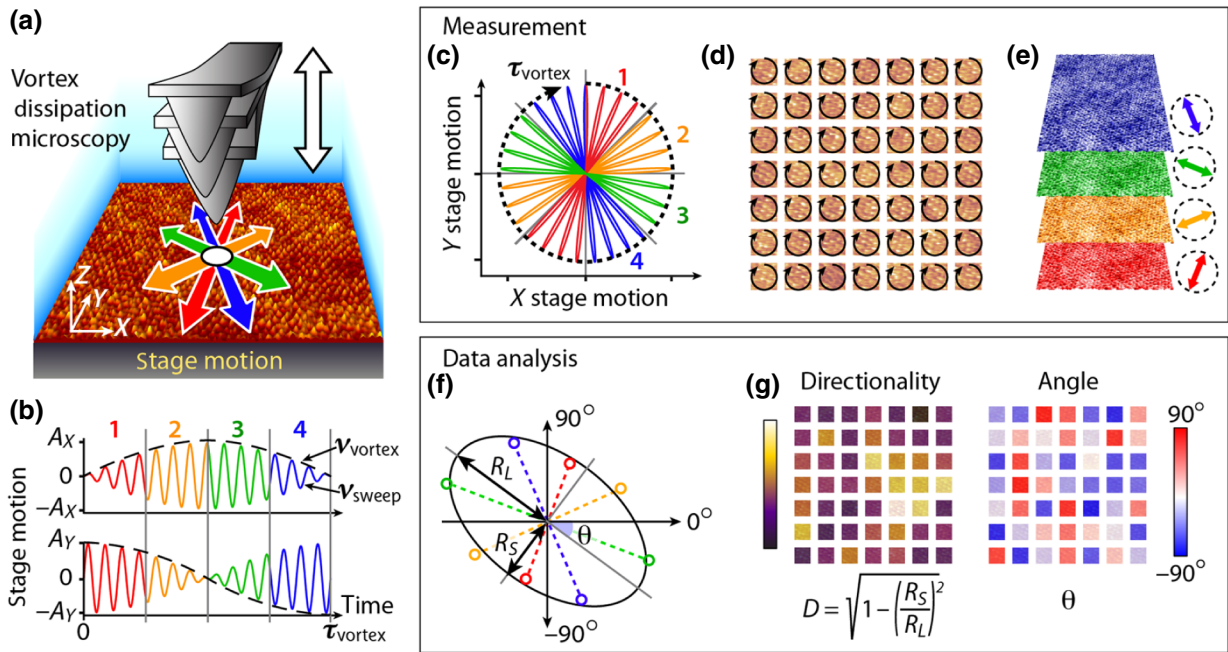


FIG. 1. Working principles of the vortex dissipation microscopy. High-resolution dynamical-mode AFM is combined with shear force microscopy to create a convoluted vertical and lateral oscillation of the tip with respect to the sample (a). The lateral oscillation (b) combines a rapid sinusoidal motion at frequency $\nu_{\text{sweep}}$ modulated by a slower frequency $\nu_{\text{vortex}}$. The resulting stage motion creates rapid lateral sweeps with slowly changing direction, probing every lateral direction around a given sample point (whole revolution or vortex) in $\tau_{\text{vortex}}$ (c). By sequencing the duration of a full vortex in a set of regular time intervals (here four) and averaging the AFM measurement parameters (amplitude, phase, frequency) over each interval, directional information can be associated with each AFM parameter for the interface location considered. The process can be repeated for each imaging pixel of the interface investigated (d), creating multiple directional charts of the lateral liquid flow (e). The data analysis is conducted pixel by pixel, plotting in polar coordinate the directional data associated with a given pixel (f). Here no phase synchronization is kept between the vertical and vortex oscillations so a given direction cannot distinguish which way (forward or backward) is preferred. Two symmetrical points are hence plotted for each direction: the angle represent the direction and the distance to origin the magnitude of the associated parameter. The polar plot is subsequently fitted with an ellipse (larger radius $R_L$, a shorter radius $R_S$, and an orientation angle $\theta$). The degree of directionality is given by the ellipse eccentricity $D = \sqrt{1 - (R_S/R_L)^2}$ with $0 \leq D \leq 1$ and $D = 0$ indicating no preferential direction. A value of $D$ and $\theta$ is obtained for each pixel (g).

ing a lateral oscillation to the sample with respect to the tip, along a controllable direction and with a velocity comparable to that of the vertical-tip motion [Fig. 1(a)]. In order to explore all the possible directions around a given location of the sample, the lateral motion is formed by two modulated oscillations along perpendicular $X$ and $Y$ directions [Fig. 1(b)]. The faster oscillation (frequency $\nu_{sweep}$) imposes a rapid lateral sweep of the tip along a given direction. The slower oscillation (frequency $\nu_{vortex}$) progressively changes the direction of the sweep, systematically exploring all the possible lateral directions over its period [Fig. 1(c)]. The resulting motion of the stage is a rapid directional sweep, which periodically rotates the direction so as to complete a full cycle over a period $\tau_{vortex}$. To reflect the vortexlike scanning motion of the stage, the method is hereafter called *vortex dissipation microscopy* (VDM).

In order to quantify the energy necessary to move the liquid in a particular direction, the energy dissipated by the tip can be calculated from the standard AFM operating parameters [39–41] directly available through the AFM controller (amplitude, phase, and frequency of the vertical oscillation), while the stage sweeps along that exact direction. The magnitude of the vertical and lateral components of the tip average velocity have to be kept comparable to ensure a meaningful directional measurement. A full directional readout is then achieved at any given location of the interface by successively quantifying the energy dissipation associated with each sweep direction over a full vortex. To do this, the vortex period is divided into smaller time windows, each associated with an average direction [time intervals 1–4 in Figs. 1(b) and 1(c)]. This strategy allows for a reasonably fast vortex acquisition while ensuring each direction is probed by multiple sweep oscillations (typically >10) for reliable measurements. The process is repeated for each pixel of the interface to map the ease with which the liquid flows in every lateral direction [Fig. 1(d)]. This results in a series of maps, each quantifying the energy dissipation associated with a given direction for each image pixel [Fig. 1(e)].

The data analysis is then conducted pixel by pixel: all the directional information associated with a given pixel is plotted in polar coordinates, with, for each direction, the angle and distance to the origin representing, respectively, the flow direction and the ease for the liquid to flow in that direction (see Appendix A for details). Subsequent fitting with an ellipse determines the dominating flow direction at the pixel considered [Fig. 1(f)]. This information is given by the ellipse eccentricity, called here directionality $D$. If the flow is equivalent in all directions, then the ellipse is a circle and $D = 0$. In contrast, if a given direction dominates, then $D > 0$ and the associated ellipse angle $\theta$ quantifies this dominating direction [Fig. 1(g)]. It should be pointed out that for values of $D$ close to zero, the angle is not reliable regardless of the fit result.

## B. Hardware development

The VDM method is, in principle, compatible with any modern AFM, provided that a lateral vortex modulation can be applied and that the data acquisition is properly synchronized so as to enable the directional analysis described above. Here, this is achieved by a purposely built piece of hardware, the "vortex scanner," made to sit directly on top of the normal AFM scanner with the sample placed on top of the vortex scanner [Fig. 2(a)]. In this way, both the standard AFM scanner and the vortex scanner can function simultaneously, with their respective motions adding up. For VDM measurements, the vortex scanner only needs to operate at two frequencies ($\nu_{sweep}$ and $\nu_{vortex}$), with a continuous modulated sinusoidal motion in both $x$ and $y$ directions, and at small amplitudes (<1 nm) to allow for high spatial resolution. It is therefore designed and built with two goals: (i) small size to fit within with most commercial AFMs and (ii) stable operation at high frequencies. The result is a small rectangular scanner of size of 12 mm × 12 mm × 2 mm [Figs. 2(b)–2(e)] with a natural resonance frequency close to 35 kHz [Fig. 2(f)]. Details of the design and calibration are discussed in Appendix B.

## C. High-resolution capabilities and no-flow reference

The main motivation for developing the VDM is to gain the ability to map interfacial flow patterns with nanoscale lateral precision. We therefore test first the impact of the VDM operation on the high-resolution capabilities of the setup in various conditions to ensure that local nanoscale measurements are possible. The mechanical properties of the interface examined are expected to significantly influence the resolution achieved [42,43] and testing is therefore conducted in aqueous solutions at the interface with a hard mica surface and a soft aquaporin 0 crystal extracted from cow lens membranes [32,44]. Furthermore, since mica exhibits a no-slip boundary condition in water [23,45], no directionality information should be observed with VDM. Representative results are presented in Fig. 3, showing the standard topography and phase information available in amplitude-modulation AFM together with the directionality and orientation (angle) data obtained from the VDM operation.

The muscovite-water interface can be resolved with atomic level resolution when the vortex scanner is switched ON (Fig. 3 upper part), revealing limited effect on the imaging quality. This is made possible by the relatively small sweeping amplitude of the vortex (here approximately 0.3 nm peak to peak based on off-resonance calibration, see Appendix B, Fig. 6). Generally, a compromise is needed between the spatial resolution achieved and deriving meaningful directional information. The former requires the sweep amplitude to be as small as possible while the latter needs for comparable vertical- and lateral-tip velocities with respect to the sample. This implies for
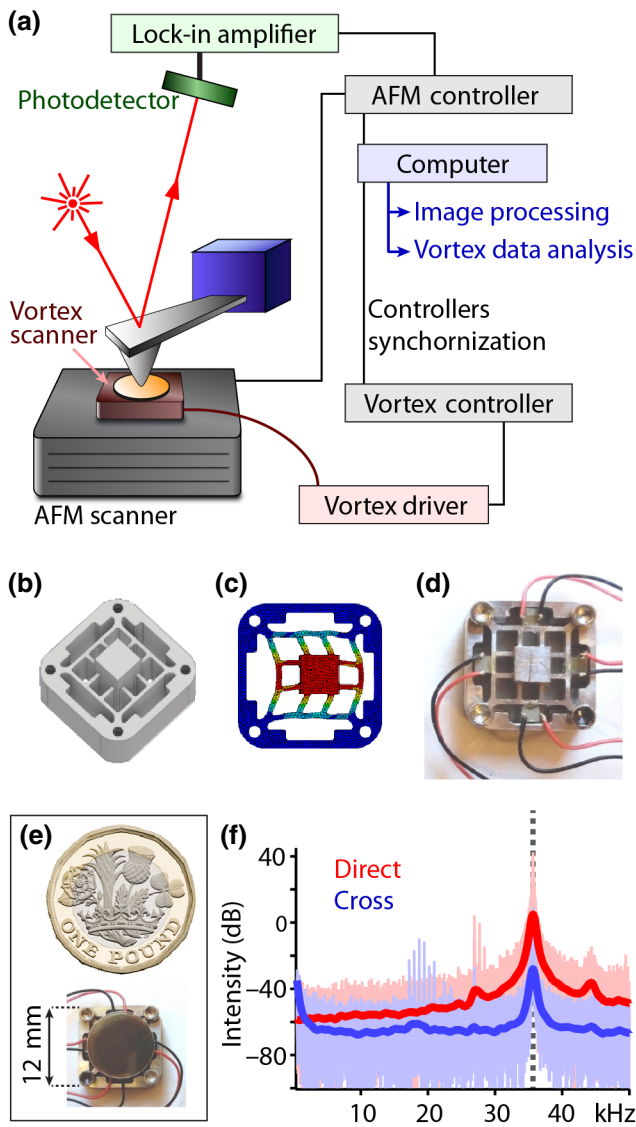
FIG. 2. Schematic representation of the VDM hardware assembly. The vortex scanner supports the sample and is mounted atop the AFM scanner (a). The electronics controlling the AFM and the VDM are synchronized to ensure completion of exactly one vortex per pixel and appropriate data acquisition. The vortex-scanner design (b) is optimized using finite-element simulation of its operation (c). The scanner realization includes $X$ and $Y$ driving piezo elements, here with counter-piezo to quantify its motion performance (d). The sample is mounted on the central part (e). The scanner size is $12 \, \text{mm} \times 12 \, \text{mm} \times 2 \, \text{mm}$, smaller than a British £1 coin (to scale). When the scanner is driven with a single piezo at 4 V and 1 Hz (f), the counter piezo and cross piezo can be used to measure, respectively, the direct (red curve) and cross-talk (blue) mechanical performance. A resonance can be seen around 35 kHz, very close to the finite elements' predicted value (dashed vertical line).

$\nu_{\text{sweep}}$ to be as large as possible, often requiring operation at frequencies higher than the vortex scanner resonance to obtain meaningful results. In practice, we find a range of

frequencies just above the scanner resonance (40–50 kHz) where acceptable resolution can be achieved for horizontal amplitudes of up to approximately 2 nm (peak to peak), almost ten times larger than the typical vertical-oscillation amplitudes. This allows us to compensate for the fact that $\nu_{\text{tip}} \sim 10 \, \nu_{\text{sweep}}$ while ensuring suitable sampling of the AFM observables. On mica, Fig. 3 shows some random fluctuations in directionality when the VDM is OFF, immediately disappearing to $D \sim 0$ when the VDM is turned ON. This is expected due to the fact that nanoscale lateral flow is negligible at the mica-water interface [23,45] (null slip length) and the VDM averages out any random fluctuations. The associated angle information is hence meaningless.

Interestingly, resolution on the aquaporin-solution interface improves when the VDM is switched ON, showing less distorted proteins and the distinctive crystal pattern in topography and phase, and the intertetramer space (smaller dashed square) appears darker in the phase as previously reported [32]. The relatively harsh imaging conditions used when the VDM is OFF come from the stiff cantilever used here, but when the VDM is switched ON the lateral-tip velocity enables the tip to "glide" on the sample's solvation layers [46], thereby preserving both sample and resolution. The directionality exhibits a faint relative increase over the intertetramer region (compared to VDM OFF) with an associated angle distribution slightly more polarized between extreme values. However, the small sampling region and the lack of proper flow calibration does not allow for any discussion beyond these qualitative observations.

We note that an ideal measurement scenario would have $\nu_{\text{tip}} = \nu_{\text{sweep}}$ and the vertical and horizontal motions synchronized in phase so as to enable not only directional information, but also differentiating between forward and backward motions of the tip in any given direction. While this is, in principle, possible, it could not be achieved with the current setup due to the lateral sweep stimulating the tip vertical oscillation in a highly directional manner when $\nu_{\text{sweep}}$ approaches the cantilever resonance frequency.

## D. Calibration of the VDM measurements

The results shown in Fig. 3 demonstrate that VMD can operate with high resolution over a variety of interfaces, but a full calibration of the system is necessary to derive meaningful quantitative data. This includes not only information from the sample, but also from the measuring tip such as the impact of the tip geometry, chemistry, and positioning (e.g., tilt angle) all of which may not be symmetrical in all lateral directions. To achieve this task, we investigate the interface between an aqueous solution and sheets of graphene oxide deposited onto an atomically flat, hydrophobic graphite (HOPG) substrate. HOPG exhibits a large slip length [23] rendering high resolution with
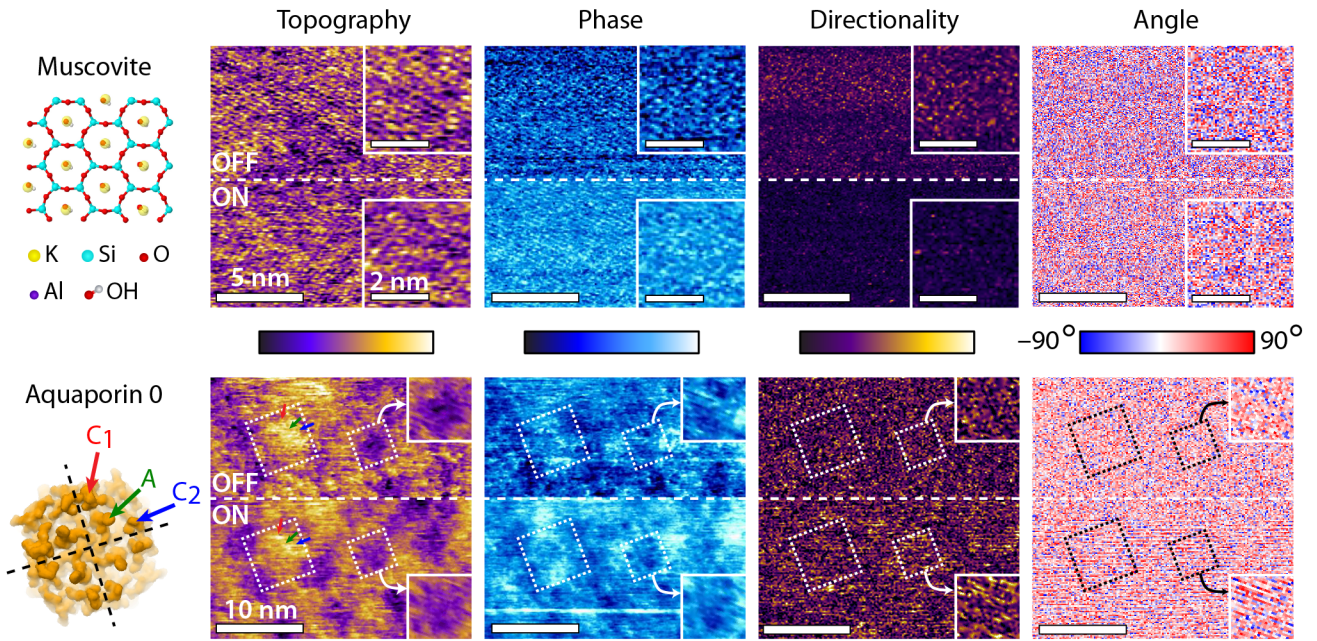
FIG. 3.   Representative examples of high-resolution VDM operation. Relatively hard (muscovite mica, top) and soft (aquaporin 0, bottom) solids are investigated in aqueous solutions. Both sets of images are acquired with the AFM scanning top to bottom and the vortex operation switched ON midimage (dashed white line) for direct comparison. Insets represent magnified portions of each image with the vortex OFF (upper) and ON (lower). A protein tetramer and an intertetramer region are highlighted on the aquaporin lattice (dashed squares). The mica is immersed in a 10-mM KCl solution and the aquaporin in Tris 10-mM, KCl 150-mM buffer solution (pH 7.4). The data on mica is acquired using a Scanasyst FLUID+ cantilever (Bruker, Coventry, UK) with a nominal stiffness $k \sim 0.7$, $\upsilon_{\text{vertical}} = 332$ kHz in solution (second eigenmode) and the vortex scanner operating with $\upsilon_{\text{sweep}} = 71.98$ kHz and $\upsilon_{\text{vortex}} = 512$ Hz. On aquaporin, the data is acquired with an Arrow UHF cantilever (Nanoworld, Neuchatel, Switzerland) with stiffness $k \sim 2$ N/m, $\upsilon_{\text{vertical}} = 303$ kHz in solution and the vortex scanner operating with $\upsilon_{\text{sweep}} = 50.176$ kHz and $\upsilon_{\text{vortex}} = 512$ Hz. The color scale bars represent height variations of 0.2 nm (mica) and 1.2 nm (aquaporin), phase variations of 20° (mica) and 10° (aquaporin), and a directionality varying between $0.01 < D < 0.45$ (mica) and $0.16 < D < 0.32$ (aquaporin).

amplitude modulation challenging [14]. Here, this can be used as a reference since the flow of water is expected to be identical all directions based on AFM observations, at least within the resolution of the VDM. In contrast, GO is hydrophilic and its ion-specific sieving capabilities [29,30] suggest the presence of directional effects in an aqueous solution. To exacerbate possible effects, the experiment is conducted in a solution of $MgCl_2$ since $Mg^{2+}$ ions are sieved out of GO filters [27], indicating strong interfacial hydration effects on flow. Since both HOPG and GO can be made atomically flat, topographical effects on the VDM measurements can be excluded. The results and their analysis are detailed in Fig. 4.

Due to atomic steps of the HOPG, it is not possible to distinguish the GO and the HOPG from the topographic information alone [Fig. 4(a)]. However, the phase exhibits a clear contrast between both materials [Fig. 4(b)]. This is expected since the phase is linked to the interfacial energy dissipation and hence sensitive to the local flow dynamics. Consistently, a lower phase (higher dissipation) is seen over the more hydrophilic GO. The directionality is also sensitive to the two materials: in the absence of vortex [Fig. 4(d) up], a marginally higher directionality is seen on

HOPG compared to GO reflecting the higher lateral flow on HOPG, albeit in random directions due to local fluctuations. When the VDM is switched ON, the measurement becomes controlled and no directionality is any longer visible on HOPG, except at step edges [bright vertical line in the lower part of Fig. 4(d)]. This apparent step directionality is however an artefact due to topographic effects and to the finite speed of the AFM feedback that induces local changes in the scanning conditions. Directionality changes at HOPG step edges are therefore ignored. In contrast, a clear and consistent directionality increase can be seen over the whole of the GO flake. The flow angle appears relatively uniform on HOPG with a bias toward positive (red) values. This bias is less marked on GO flakes. To better quantify the differences in angle between GO and HOPG, we use the phase information [Fig. 4(b)] to create a mask that objectively distinguishes GO and HOPG and calculate angle probability distributions on both regions [Figs. 4(f) and 4(g)]. The angle distribution exhibits a clear maximum on HOPG despite no topographical effects, pointing to tip effects instead. The measuring tip is bound to affect the measurement by the fact that it is not perfect with some asymmetry in shape, chemistry, hydration, and
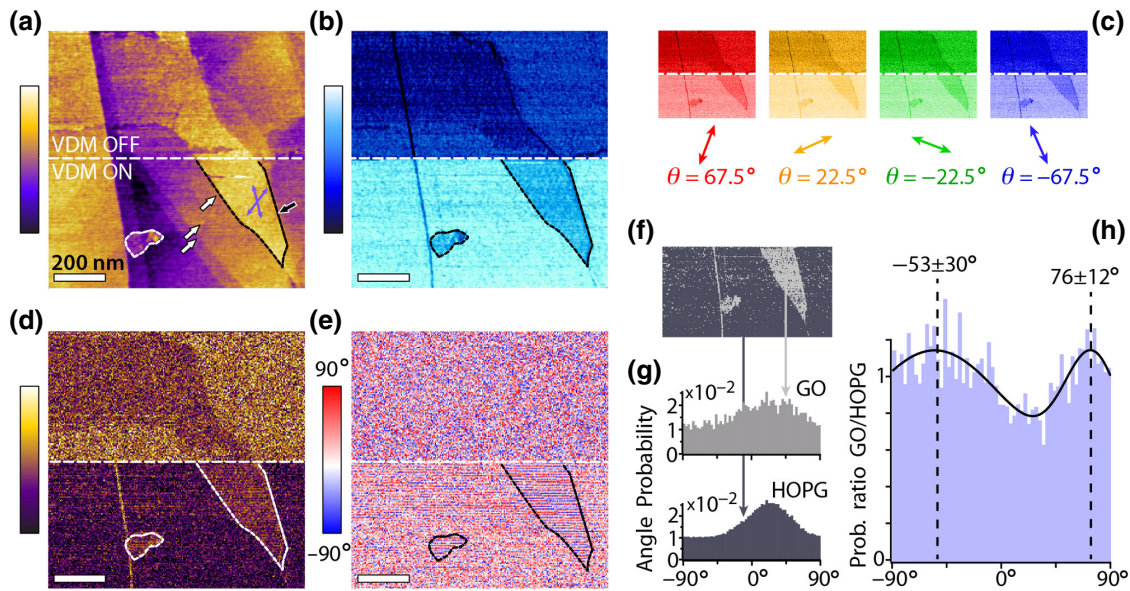
FIG. 4.    VDM analysis of the interface between a GO flake and a 10-mM MgCl$_2$ solution. As for Fig. 3, the vortex scanner is switched ON halfway through the AFM scan so that the top part of all images (VDM OFF) serves as reference. Topography (a) and phase images (b) show GO flakes (black dashed outline) on top of the HOPG surface. HOPG atomic steps are indicated with the white arrows and the edge of the GO flake with a black arrow in (a). Interestingly, the phase contrast between GO and HOPG is enhanced by the VDM with a darker phase over the GO. This confirms a high dissipation over GO and hence lower slippage or ease for the solution to flow. Using the VDM acquisition and analysis strategy described in Fig. 1, directional flow maps are acquired (c) and combined into directionality (d) and angle (e) images. GO flakes exhibit a higher directionality than HOPG and a lower (bluer) angle probability. A mask based on the phase contrast (f) is used to sample the angle distributions over HOPG and GO regions (g). The angle distribution over HOPG shows one clear maximum around 30°, presumably induced by tip effects such as vertical tilt and local chemistry. The distribution broadens and shifts towards lower angles over GO. Normalizing the GO distribution by the HOPG distribution provides a result free of tip effects (h). Two maxima are visible at approximately 120° from each other, obtained by fitting the normalized distribution with a sum of two Gaussians. The corresponding directions are indicated by purple arrows in (a), suggesting an alignment with the GO flake edge and its crystalline orientation. The data is acquired using a Scanasyst FLUID+ cantilever with $v_{vertical} = 305$ kHz in solution (second eigenmode) and the vortex scanner operating with $v_{sweep} = 40.96$ kHz and $v_{vortex} = 512$ Hz. The color scale bars represent height variations of 3 nm (a), phase variations of 30° (b), and a directionality varying between $0.15 < D < 0.45$ (d).

potentially also in its positioning with a likely tilt of the tip axis with respect to the interface's perpendicular direction. The measurement on HOPG therefore serves as a calibration to quantify this effect and exclude them from further measurements. Here, this is done for GO by dividing the angle distribution obtained on GO by that on HOPG [Fig. 4(h)]. Two distinct maxima appear at approximately 120° from each other [purple arrows in (a)] and aligned with the edge of the GO flake (black arrow). This clearly suggests a correlation between the preferential flow directions and the crystalline orientation of the GO. Significantly, the preferred directions are not well aligned with the HOPG's atomic steps [white arrows in (a)], reinforcing the interpretation that GO dominates the flow pattern.

### E. Nanoscale flow patterns in different ionic solutions

To further confirm the VDM results, the same experiment is conducted in a 10-mM KCl solution, with the same AFM tip, in the same operating conditions, and over the same sample location. To avoid possible cross-contamination, the experiment is first conducted in KCl and subsequently in MgCl$_2$ with the latter presented in Fig. 3. A comparative result for both ionic solutions is given in Fig. 5.

Standard amplitude-modulation AFM gives almost identical results in KCl and in MgCl$_2$, but the VDM analysis shows significant differences in interfacial flow when Mg$^{2+}$ ions are present in the solution. In KCl, no change in directionality can be seen between HOPG and GO, a result confirmed by the absence of any preferred angle once the tip effects have been discounted. However, preferential flow directions in registry with the GO lattice emerge in the presence of Mg$^{2+}$ ions. To understand the origin of these ion-specific differences, it is worth considering the hydrodynamic radii of the two cations with 3.31 Å for K$^+$ and 4.28 Å for Mg$^{2+}$ [27,47]. Previous studies have shown the hydrodynamic radius of the cations present in solution to play a key role on their intercalation and percolation between GO flakes and determine the sieving performance of GO membranes [27,29,30]. The permeation rate is significantly larger for K$^+$ than for
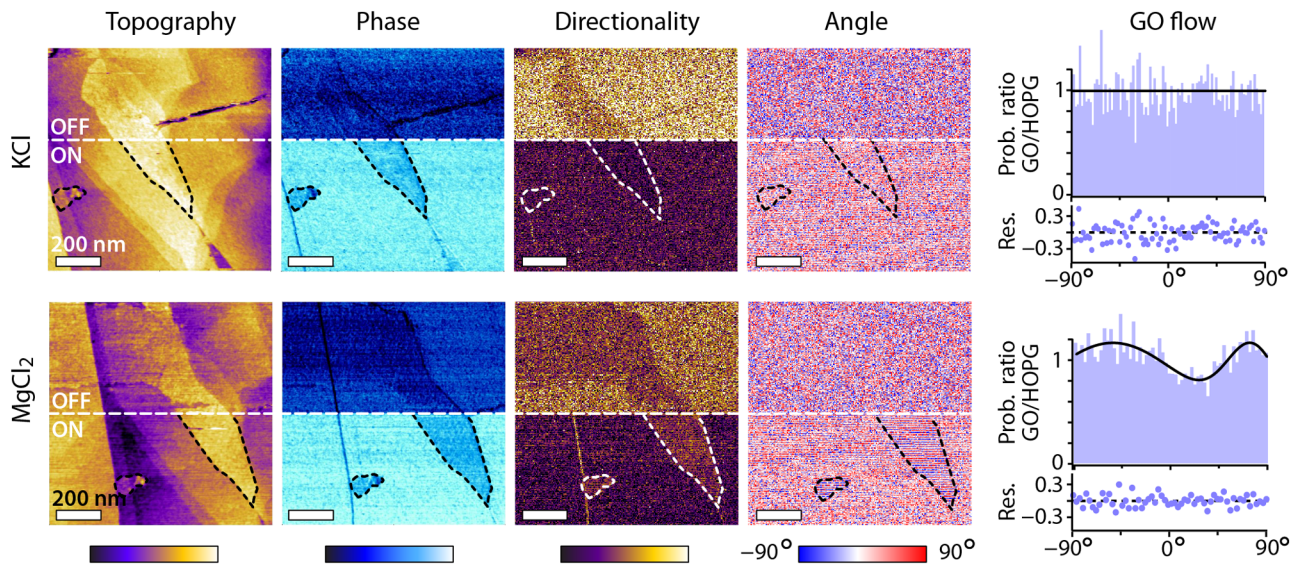
FIG. 5. Comparative VDM results for a same GO flake in a solution of KCl and $MgCl_2$. The same sample location is investigated in both cases, in identical operating conditions and with the same tip. The results are acquired first in 10-mM KCl and subsequently in 10-mM $MgCl_2$ after extensively rinsing the sample with the $MgCl_2$ solution. The phase contrast between GO and HOPG is consistent and similar in magnitude in both solutions, but no clear directionality contrast can be seen in KCl. Similarly, no preferential angle can be identified in the KCl solution. The angle distribution is fitted with a horizontal line in KCl and a double Gaussian in $MgCl_2$, with the fit residuals given in both cases. The data is presented as in Fig. 4 and is identical for $MgCl_2$. The color scale bars are identical for both solutions and represent height variations of 3 nm (topography), 30° (phase), and $0.15 < D < 0.45$ (directionality).

$Mg^{2+}$ [27,28] with a total permeation cutoff for ions with hydrodynamic radii larger than approximately 4.5 Å [29]. Since GO membranes are typically composed of random stacks of GO flakes, reliable measurements of the permeation rates are challenging and results can be contradictory depending on the membrane preparation [48–50]. Generally, the permeation is explained in terms of geometrical constraints whereby larger ions and molecules simply cannot pass in the limited space available between adjacent GO sheets [30,51–53]. Electrostatic interactions between the moving ions and the GO's carbonyl groups have also been invoked to explain the swelling of GO stacks in the presence of $MgCl_2$ [31].

The present results suggest that the motion of metal ions at the surface of GO can be understood as a combination of restructuring dynamics of the water molecules between the ions' shell and the GO's hydrophilic groups, and direct electrostatic interactions between ions and the GO surface. The effect of hydration water on the dynamics of the ions is expected from previous studies with GO [29]. Water molecules have been shown to move at superdiffusive velocities between GO sheets by primarily traveling on hydrophobic paths and avoiding GO's hydrophilic groups and flowing [54]. Adding hydrated ions to the system can partly be explained by the same picture whereby larger ions can no longer travel along these hydrophobic paths without interacting with GO's hydrophilic groups or shedding part of their hydration water to fit between GO sheets [29,30].

In this framework, the size dependence on the hydrated ions' radius can be explained with a combination of enthalpic and entropic free energy costs. Larger hydrated ions are usually more densely charged and experience stronger electrostatic interactions with the negatively charged GO surface. Moving along the interface therefore incurs higher enthalpic costs for larger ions, which are more likely to remain in registry with the underlying GO lattice. The effect is further exacerbated by the low dielectric constant of nanoconfined water [55]. The entropy costs associated with the ions moving along the interface originate from the restructuring of water molecules in the ion's and GO's hydration shell. Size-related effects are likely to depend on the degree of confinement [56] and are hence less straightforward to predict than enthalpic contributions.

Similar experiments have been conducted with AFM to investigate the behavior of metal cations at the interface with mica in aqueous solutions [9,57]. Mica surfaces are atomically flat over large regions and exhibit a hexagonal lattice with a periodicity close to double that of graphene. In the present experimental conditions, mica is negatively charged with a surface potential of the order of –60 to –80 mV [58], about twice the value of GO [36]. When minimally confined (as is the case here), metal cations diffusing at the surface of mica show little dependence on temperature [57], confirming enthalpic effects to dominate. This is to be expected considering the larger surface potential. However, in case of a strong confinement with an AFM tip during shear experiments, the hydrogen bond

network formed by the interfacial water molecules dominate the cation's mobility, with divalent cations moving more easily owing to their ability to better disrupt the local hydrogen bond order [9]. While experiments conducted on mica cannot be directly transposed to the present case with mica being almost defect-free and able to stabilize interfacial water molecules in an ice-like arrangement [57,59], the fact that the opposite trend is observed here on GO suggests that enthalpic effects involving direct electrostatic interactions between the ions and the charged groups of the GO surface dominate. This is also supported by the fact that densely charged $Mg^{2+}$ ions tend to move more easily when in registry with the underlying crystalline lattice.

Overall, the VDM results are consistent with the well-known poor permeability of typical GO membranes to $Mg^{2+}$ ions and the variability between different permeability measurements [27,29,48]: the existence of a clear preferential direction for ions moving between two GO sheets hinges on the sheets having their respective lattice in registry. This is unlikely to be the case for most GO membranes unless created so by design.

### F. General discussion and conclusion

The present study describes how AFM operation in liquid augmented with small lateral oscillations can be used to map the nanoscale flow patterns naturally adopted by the liquid parallel to the surface of immersed solids. The method is compatible with most existing AFMs and exploits the boundary friction of the interfacial liquid when pushed in a given direction to quantitatively deduce the ease for the liquid to move in the direction considered. The VDM method builds on the fact that AFM measurements conducted within the interfacial liquid are highly sensitive to the boundary flow through the measured energy dissipation [14,23,42]. In order to derive meaningful flow information, most of the tip apex ($>20$ nm$^2$) is likely to contribute to the measured dissipation, but atomic level resolution is still possible thanks to localized asperities [14,60] or stable hydration sites [61] located on the tip apex. Here, the validity of the VDM approach is demonstrated on reference samples such as mica and HOPG where no measurable directionality is expected. On mica, the boundary slip is known to be zero [23], hence preventing lateral flow in any direction. On HOPG, the boundary slip is relatively large, but AFM cannot identify any specific feature or preferred direction when operated as in the present study. Consistently, VDM measures zero directionality on mica, and a small directionality on HOPG, the latter being due to expected tip effects that can subsequently be discounted.

Our results demonstrate that the approach is also compatible with high-resolution imaging and can be exploited to gain insights into the nanoscale fluid dynamics at interfaces. Quantitative measurements taken on GO membranes illustrate directly and *in situ* the ion-dependent directional flow effects. While such effects are known to occur, the present results provide insights into the underpinning molecular mechanisms and suggest that electrostatic interactions through the hydration water may dominate the process over equilibrium steric effects. Arguably, the images (Figs. 4 and 5) are relatively low resolution when compared to those presented in Fig. 3, but this is due to the emphasis being placed on obtaining quantitative directional information and on reproducibility. Higher resolution is also possible on the HOPG and GO systems when relaxing the requirement of using the same tip over the same sample location, with details of the interface resolved down to the nanometer level (Appendix C, Fig. 7).

Beyond the measurements rendered possible here with the VDM, there is still scope for improvement and exploration of the method's possibilities. The vortex scanner, for example, can be improved for higher resonance and lower noise operation, for example by operating the acquisition off resonance [22] to avoid cross-talk between lateral and vertical oscillations. In terms of the measurement process itself, the VDM can be exploited to modulate and enhance the spatial resolution and explore the dynamics of different solvation layers at interfaces, as illustrated in Fig. 3 over aquaporin. This is because the interfacial liquid itself plays an important role in AFM resolution at solid-liquid interfaces [14,43]. On soft samples such as biomembranes this can be further exploited to preserve the sample by playing with the viscoelastic properties of the interfacial water, which then acts as a lubrication, energy-absorbing layer [62]. Future work will explore the full capabilities of VDM, in particular on biological samples where membrane fluidity [63], interfacial molecular diffusion, and biomolecular dynamics [4,5,32] are closely related to the properties of interfacial liquid.

### APPENDIX A: FROM DIRECTIONAL EXPERIMENTAL PARAMETERS TO FLOW PATTERNS

In order to calculate flow patterns from directional experimental parameters, it is necessary to know how the

parameter considered relates to local energy dissipation [14,39,40], itself an indicator of the ease with which the liquid can flow along the interface [23,26]. Here, local energy dissipation can be calculated from the amplitude and the phase of the vertical-tip oscillation [39,40]. Since the amplitude is kept constant (amplitude modulation), in first approximation the energy dissipated by the tip varies with the sine of the phase [40]. The flow pattern is determined by comparing the magnitude of the energy dissipation in all directions; directions with comparatively lower dissipation are the more probable, while directions associated with higher dissipation are less likely. Since the measurement is comparative, determining the exact value of the dissipation is not necessary provided the parameter examined for a given pixel varies monotonically with the dissipation. Here we simply use the imaging phase, taking an arbitrary reference so that when plotted in polar coordinates (Fig. 1), the direction with the highest phase (highest dissipation) is located closest to the center of the ellipse. No dependence of the observed trends on the reference chosen can be found, provided it satisfies the above criterion. Typically, difference references affect the magnitude of the fitted ellipse eccentricity, but the directionality image remains unchanged.

## APPENDIX B: DESIGN, CALIBRATION, AND OPERATION OF THE VORTEX SCANNER

### Design and operation

The vortex scanner needs to operate at relatively high frequencies with $\nu_{sweep}$ close in value to $\nu_{tip}$. This makes its development challenging from a hardware perspective, especially considering the high-resolution requirements of VDM. Typical AFMs have mechanical resonances below 5 kHz. In contrast, cantilever and tips routinely used for high-resolution imaging in liquid typically operate over frequencies $\nu_{tip} \sim 20 - 500$ kHz in solution. Additionally, the vortex scanner needs to satisfy strict size constraints to fit in compact commercial AFMs such as here the Cypher ES (Asylum Research).

To satisfy these constraints the vortex scanner is designed following a number of iterations using detailed modal analysis using finite-element analysis (FEA) to model the behavior of the vortex scanner and calculate its resonance frequency depending on designs and composing materials. The geometry shown in Fig. 2 is retained, composed of aluminum 7075.

Actuation of the stage is ensured by four piezoelectric stack actuators (miniature multilayer piezo actuators PL022.3x PICMA, Physik Instrumente, Karlsruhe, Germany). The piezo actuators are driven directly by a Data Acquisition Board (NI USB-6366, X Series DAQ Device, National Instruments, Austin, TX, USA). Since VDM requires only small amplitude lateral oscillations,

the voltages applied to the piezo actuators rarely exceed 1–2 V, bypassing the need for an amplifier.

The first resonance frequency of the scanner can be measured experimentally, by driving a single piezo actuator with a random noise centered around low-frequency signals with 4-V amplitude and recording the resulting displacement with the counter and cross actuators.

Control of the vortex scanner is ensured using bespoke routines programmed using the Laboratory Virtual Instrument Engineering Workbench (LabVIEW, National Instruments). VDM data acquisition is achieved through the same DAQ as the vortex scanner, with the raw phase signal extracted directly from the AFM and recorded in LabVIEW at 2 MHz, relying on triggers from the AFM acquisition software (Igor Pro, Wavemetrics, OR, USA) to ensure synchronization of the AFM and VDM data. Subsequent VDM data analysis and time averaging over the selected number of directions (Fig. 1) is conducted *a posteriori*, using routines programmed in Matlab (Mathworks, Cambridge, UK).

### Calibration

To calibrate the vortex scanner and determine its oscillation amplitude in nanometers, it is necessary to use a known reference sample. We select mica for its well-characterized hexagonal lattice with 0.52-nm periodicity [64,65]. The calibration is carried out by operating the vortex scanner as a standard AFM scanner so as to correlate the applied voltage with the number of mica lattice cells scanned. This is done independently for both scanning directions ($X$ and $Y$).

Practically, for a given scanning direction the vortex scanner is operated to oscillate sinusoidally along that direction at low frequency (1–2 Hz) and with different
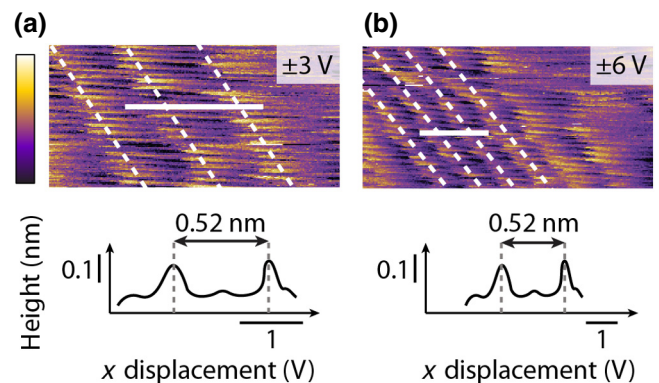


FIG. 6.    Calibration of the vortex scanner. Images are acquired using only the vortex scanner motion (here $x$ axis) with a voltage amplitude of $\pm 3$ V (a) and $\pm 6$ V for (b). The mica lattice (dashed white lines) acts as a calibration grid due to its known periodicity, with height profiles (white line) yielding the desired calibration ratio in V/nm. The color scale bar represents height variations of 0.2 nm.
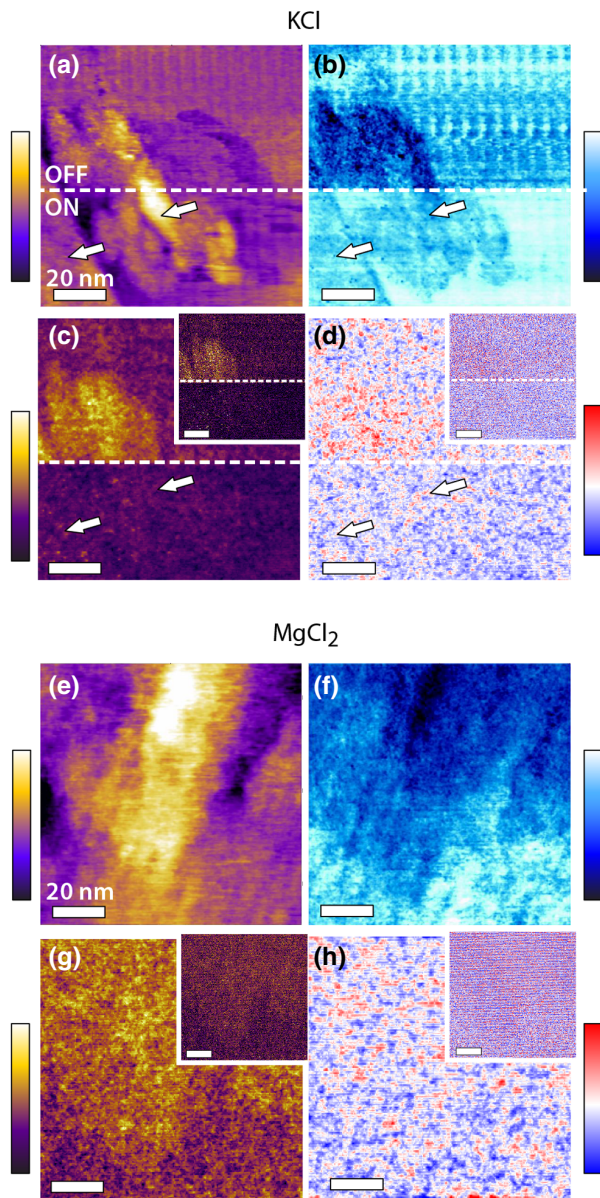
KCl



MgCl$_2$

FIG. 7.    High-resolution VDM on GO in KCl and MgCl$_2$. Images are presented in the same order as in Fig. 4 with topography (a), (e), phase (b), (f), directionality (c), (g), and angle (d), (h). To enhance the fine details and remove the VDM noise, the VDM data in both solutions is low-pass filtered, with the original raw data in the insert in each case. In KCl (a)–(d), a contrast between GO and HOPG is visible in phase (b) at the edge of a graphite flake (white arrows) but no directionality (c) is present once the VDM is switched ON. In MgCl$_2$ (e)–(h), with VDM switched ON for the whole image, some fine details can be seen in directionality after filtering (g). The details are not induced by the filtering but confirmed by the same level of detail visible in the phase (f). The angle data also reveal some consistent variations across the sample. Color scale bars represent height variations of 1.5 and 3 nm (topography in KCl and MgCl$_2$, respectively), 15° and 20° (phase in KCl and MgCl$_2$, respectively), $0.1 < D < 0.45$ (unfiltered directionality), and $-15° < \theta < 20°$ (angle). The color scale on the filtered data enhances the contrasts as much as possible.

amplitudes. The data acquisition is conducted directly by the AFM, imposing the same scanning rate on the AFM scanner but with a scan size of 0 nm. A typical calibration image set is presented in Fig. 6. The image represents the same profile scanned repeatedly. Since the scanning tip does not move in perfect registry with the lattice (not perfectly aligned), the lattice profile appears to be linearly shifting in time due to small positional drift.

## Operation and data acquisition

In order to derive meaningful VDM information, comparable vertical- and lateral-tip velocities with respect to the sample are needed. This implies for $v_{sweep}$ to be as large as possible, often requiring operation at frequencies higher than the vortex-scanner resonance to obtain meaningful results. In practice, we find a range of frequencies just above the scanner resonance (40–50 kHz) where acceptable resolution can be achieved for horizontal amplitudes of up to approximately 2 nm (peak to peak), almost ten times larger than the typical vertical-oscillation amplitudes. This allows us to compensate for the fact that $v_{tip} \sim 10\, v_{sweep}$ while ensuring suitable sampling of the AFM observables.

We note that in an ideal measurement scenario, $v_{tip} = v_{sweep}$ and the vertical and horizontal motions are synchronized in phase so as to enable not only directional information, but also differentiating between forward and backward motions of the tip in any given direction. This is, however, not possible with the current setup due to the lateral sweep stimulating the tip vertical oscillation (cantilever resonance) in a highly directional manner.

## APPENDIX C: HIGH-RESOLUTION VDM ON GO

It is possible to obtain nanometer-level information on GO and HOPG with VDM (Fig. 7). When focusing on high resolution, it is often necessary to acquire multiple images in order to optimize the VDM operating parameters. This makes it challenging to use the same cantilever and tip for multiple sets of measurements and the representative data presented in Fig. 7 is acquired with different cantilevers in KCl and MgCl$_2$. Some directionality is visible with AFM in KCl, but it vanishes when the VDM is switched ON.

[1] W. Kaplan and Y. Kauffmann, Structural order in liquids induced by interfaces with crystals, Annu. Rev. Mater. Res. **36**, 1 (2006).

[2] C. Yu, G. Evmenenko, A. Richter, A. Datta, J. Kmetko, and P. Dutta, Order in molecular liquids near solid-liquid interfaces, Appl. Surf. Sci. **182**, 231 (2001).

[3] P. Fenter and N. Sturchio, Mineral-water interfacial structures revealed by synchrotron x-ray scattering, Prog. Surf. Sci. **77**, 171 (2004).

[4] H. Frauenfelder, G. Chena, J. Berendzena, P. W. Fenimore, H. Janssonb, B. H. McMahon, I. R. Stroe, J. Swenson, and R. D. Young, A unified model of protein dynamics, Proc. Natl. Acad. Sci. U.S.A. **106**, 5129 (2009).

[5] M. Grossman, B. Born, M. Heyden, D. Tworowski, G. B. Fields, I. Sagi, and M. Havenith, Correlated structural kinetics and retarded solvent dynamics at the metalloprotease active site, Nat. Struct. Mol. Biol. **18**, 1102 (2011).

[6] K. Voïtchovsky, D. Giofrè, J. José Segura, F. Stellacci, and M. Ceriotti, Thermally-nucleated self-assembly of water and alcohol into stable structures at hydrophobic interfaces, Nat. Commun. **7**, 13064 (2016).

[7] J. Love, L. Estroff, J. Kriebel, R. Nuzzo, and G. Whitesides, Self-assembled monolayers of thiolates on metals as a form of nanotechnology, Chem. Rev. **105**, 1103 (2005).

[8] L. Gao and T. McCarthy, Wetting 101°, Langmuir **25**, 14105 (2009).

[9] C. Cafolla and K. Voïtchovsky, Lubricating properties of single metal ions at interfaces, Nanoscale **10**, 11831 (2018).

[10] U. F. Keyser, B. N. Koeleman, S. van Dorp, D. Krapf, R. M. M. Smeets, S. G. Lemay, N. H. Dekker, and C. Dekker, Direct force measurements on DNA in a solid-state nanopore, Nat. Phys. **2**, 473 (2006).

[11] M. Kühne, F. Börrnert, S. Fecher, M. Ghorbani-Asl, J. Biskupek, D. Samuelis, A. V. Krasheninnikov, U. Kaiser, and J. H. Smet, Reversible superdense ordering of lithium between two graphene sheets, Nature **564**, 234 (2018).

[12] K. Voïtchovsky, N. Ashari-Astani, I. Tavernelli, N. Tetreault, U. Rothlisberger, F. Stellacci, M. Grätzel, and H. A. Harms, In situ mapping of the molecular arrangement of amphiphilic Dye molecules at the $TiO_2$ surface of Dye-sensitized solar cells, ACS Appl. Mater. Interf. **7**, 10834 (2015).

[13] T. Fukuma, M. Higgins, and S. Jarvis, Direct Imaging of Lipid-Ion Network Formation Under Physiological Conditions by Frequency Modulation Atomic Force Microscopy, Phys. Rev. Lett. **98**, 106101 (2007).

[14] K. Voïtchovsky, J. J. Kuna, S. A. Contera, E. Tosatti, and F. Stellacci, Direct mapping of the solid-liquid adhesion energy with subnanometre resolution, Nat. Nanotechnol. **5**, 401 (2010).

[15] W. Trewby, J. Faraudo, and K. Voïtchovsky, Long-lived ionic nano-domains can modulate the stiffness of soft interfaces, Nanoscale **284**, 173 (2019).

[16] T. Fukuma, Y. Ueda, S. Yoshioka, and H. Asakawa, Atomic-Scale Distribution of Water Molecules at the Mica-Water Interface Visualized by Three-Dimensional Scanning Force Microscopy, Phys. Rev. Lett. **104**, 016101 (2010).

[17] D. Martin-Jimenez, E. Chacon, P. Tarazona, and R. Garcia, Atomically resolved three-dimensional structures of electrolyte aqueous solutions near a solid surface, Nat. Commun. **7**, 12164 (2016).

[18] X. Xiong, S. Guo, Z. Xu, P. Sheng, and P. Tong, Development of an atomic-force-microscope-based hanging-fiber rheometer for interfacial microrheology, Phys. Rev. E **80**, 061604 (2009).

[19] D. Guan, E. Charlaix, R. Z. Qi, and P. Tong, Noncontact Viscoelastic Imaging of Living Cells Using a Long-Needle Atomic Force Microscope with Dual-Frequency Modulation, Phys. Rev. Appl. **8**, 044010 (2017).

[20] T. Uchihashi, N. Kodera, and T. Ando, Guide to video recording of structure dynamics and dynamic processes of proteins by high-speed atomic force microscopy, Nat. Protoc. **7**, 1193 (2012).

[21] T. Uchihashi, R. Iino, T. Ando, and H. Noji, High-Speed atomic force microscopy reveals rotary catalysis of rotorless F1-ATPase, Science **333**, 755 (2011).

[22] A. P. Nievergelt, N. Banterle, S. H. Andany, P. Gönczy, and G. E. Fantner, High-speed photothermal off-resonance atomic force microscopy reveals assembly routes of centriolar scaffold protein SAS-6, Nat. Nanotechnol. **13**, 696 (2018).

[23] D. Ortiz-Young, H. C. Chiu, S. Kim, K. Voïtchovsky, and E. Riedo, The interplay between apparent viscosity and wettability in nanoconfined water, Nat. Commun. **4**, 2482 (2013).

[24] C.-L. M. H. Navier, Mémoire sur les lois de l'équilibre et du mouvement des corps solides élastiques, Mém. Acad. Roy. Sci. Inst. France. **7**, 375 (1927).

[25] L. R. Bocquet and J.-L. Barrat, Flow boundary conditions from nano- to micro-scales, Soft Matter **3**, 685 (2007).

[26] D. M. Huang, C. Sendner, D. Horinek, R. R. Netz, and L. Bocquet, Water Slippage Versus Contact Angle: A Quasiuniversal Relationship, Phys. Rev. Lett. **101**, 226101 (2008).

[27] J. Abraham, K. S. Vasu, C. D. Williams, K. Gopinadhan, Y. Su, C. T. Cherian, J. Dix, E. Prestat, S. J. Haigh, I. V. Grigorieva, P. Carbone, A. K. Geim, and R. R. Nair, Tunable sieving of ions using graphene oxide membranes, Nat. Nanotechnol. **12**, 546 (2017).

[28] J.-H. Song, H.-W. Yu, M.-H. Ham, and I. S. Kim, Tunable Ion sieving of graphene membranes through the control of nitrogen-bonding configuration, Nano Lett. **18**, 5506 (2018).

[29] R. K. Joshi, P. Carbone, F. C. Wang, V. G. Kravets, Y. Su, I. V. Grigorieva, H. A. Wu, A. K. Geim, and R. R. Nair, Precise and ultrafast molecular sieving through graphene oxide membranes, Science **343**, 752 (2014).

[30] B. Mi, Graphene oxide membranes for ionic and molecular sieving, Science **343**, 740 (2014).

[31] Y. Mo, X. Zhao, and Y.-X. Shen, Cation-dependent structural instability of graphene oxide membranes and its effect on membrane separation performance, Desalination **399**, 40 (2016).

[32] M. Ricci, R. A. Quinlan, and K. Voïtchovsky, Sub-nanometre mapping of the aquaporin–water interface using multifrequency atomic force microscopy, Soft Matter **13**, 187 (2017).

[33] N. I. Kovtyukhova, P. J. Ollivier, B. R. Martin, T. E. Mallouk, S. A. Chizhik, E. V. Buzaneva, and A. D. Gorchinskiy, Layer-by-Layer assembly of ultrathin composite films from micron-sized graphite oxide sheets and polycations, Chem. Mater. **11**, 771 (1999).

[34] W. Hummers and R. Offeman, Preparation of graphitic oxide, J. Am. Chem. Soc. **80**, 1339 (1958).

[35] J. Zhong, W. Sun, Q. Wei, X. Qian, H.-M. Cheng, and W. Ren, Efficient and scalable synthesis of highly aligned and compact two-dimensional nanosheet films with record performances, Nat. Commun. **9**, 1 (2018).

[36] G. Xu, J. Zhong, and X. Shi, Influence of graphene oxide in a chemically activated fly ash, Fuel **226**, 644 (2018).

[37] Y. Yu, J. Zhong, W. Sun, R. Kumar, and N. Koratkar, Solid-State hybrid fibrous supercapacitors produced by dead-End tube membrane ultrafiltration, Adv. Funct. Mater. **27,** 1606461 (2017).

[38] E. J. Miller, W. Trewby, A. Farokh Payam, L. Piantanida, C. Cafolla, and K. Voïtchovsky, Sub-nanometer resolution imaging with amplitude-modulation atomic force microscopy in liquid, J. Vis. Exp. **118,** e54924 (2016).

[39] H. Söngen, R. Bechstein, and A. Kühnle, Quantitative atomic force microscopy, J. Phys.: Condens. Matter **29,** 274001 (2017).

[40] J. Cleveland, B. Anczykowski, A. Schmid, and V. Elings, Energy dissipation in tapping-mode atomic force microscopy, Appl. Phys. Lett. **72,** 2613 (1998).

[41] J. Sader and S. Jarvis, Coupling of conservative and dissipative forces in frequency-modulation atomic force microscopy, Phys. Rev. B **74,** 195424 (2006).

[42] K. Voïtchovsky, Anharmonicity, solvation forces, and resolution in atomic force microscopy at the solid-liquid interface, phys, Rev. E **88,** 022407 (2013).

[43] K. Voïtchovsky and M. Ricci, in *Proc. SPIE*, edited by W. J. Parak, K. Yamamoto, M. Osinski (SPIE, San Francisco, California, USA, 2012), pp. 82320O–8.

[44] N. Buzhynskyy, P. Sens, F. Behar-Cohen, and S. Scheuring, Eye lens membrane junctional microdomains: A comparison between healthy and pathological cases, New J. Phys. **13,** 085016 (2011).

[45] T.-D. Li and E. Riedo, Nonlinear Viscoelastic Dynamics of Nanoconfined Wetting Liquids, Phys. Rev. Lett. **100,** 106102 (2008).

[46] A. Humphris, M. Miles, and J. Hobbs, A mechanical microscope: High-speed atomic force microscopy, Appl. Phys. Lett. **86,** 034106 (2005).

[47] J. Mähler and I. Persson, A study of the hydration of the alkali metal ions in aqueous solution, Inorg. Chem. **51,** 425 (2011).

[48] A. Morelos-Gomez, R. Cruz-Silva, H. Muramatsu, J. Ortiz-Medina, T. Araki, T. Fukuyo, S. Tejima, K. Takeuchi, T. Hayashi, M. Terrones, and M. Endo, Effective NaCl and dye rejection of hybrid graphene oxide/graphene layered membranes, Nat. Nanotechnol. **12,** 1083 (2017).

[49] Z. Jia, W. Shi, Y. Wang, and J. Wang, Dicarboxylic acids crosslinked graphene oxide membranes for salt solution permeation, Coll. Surf., A **494,** 101 (2016).

[50] J. Wang, L. Zhao, D. Wei, W. Wu, J. Zhang, and X. Cheng, Effects of intercalated molecules in graphene oxide on the interlayer channels for anhydrous proton conduction, Ind. Eng. Chem. Res. **55,** 11931 (2016).

[51] L. Huang, Y. Li, Q. Zhou, W. Yuan, and G. Shi, Graphene oxide membranes with tunable semipermeability in organic solvents, Adv. Mater. **27,** 3797 (2015).

[52] A. Klechikov, J. Yu, D. Thomas, T. Sharifi, and A. V. Talyzin, Structure of graphene oxide membranes in solvents and solutions, Nanoscale **7,** 15374 (2015).

[53] A. V. Talyzin, T. Hausmaninger, S. You, and T. Szabó, The structure of graphene oxide membranes in liquid water, ethanol and water–ethanol mixtures, Nanoscale **6,** 272 (2014).

[54] D. W. Boukhvalov, M. I. Katsnelson, and Y.-W. Son, Origin of anomalous water permeation through graphene oxide membrane, Nano Lett. **13,** 3930 (2013).

[55] L. Fumagalli, A. Esfandiar, R. Fabregas, S. Hu, P. Ares, A. Janardanan, Q. Yang, B. Radha, T. Taniguchi, K. Watanabe, G. Gomila, K. S. Novoselov, and A. K. Geim, Anomalously low dielectric constant of confined water, Science **360,** 1339 (2018).

[56] D. Argyris, D. R. Cole, and A. Striolo, Ion-Specific effects under confinement: The role of interfacial water, ACS Nano **4,** 2035 (2012).

[57] M. Ricci, W. Trewby, C. Cafolla, and K. Voïtchovsky, Direct observation of the dynamics of single metal ions at the interface with solids in aqueous solutions, Sci. Rep. **7,** 43234 (2017).

[58] Z. Adamczyk, M. Zaucha, and M. Zembala, Zeta potential of mica covered by colloid particles: A streaming potential study, Langmuir **26,** 9368 (2010).

[59] Y. Leng and P. T. Cummings, Fluidity of Hydration Layers Nanoconfined Between Mica Surfaces, Phys. Rev. Lett. **94,** 026101 (2005).

[60] D. J. Müller, D. Fotiadis, S. Scheuring, S. A. Müller, and A. Engel, Electrostatically balanced subnanometer imaging of biological specimens by atomic force microscope, Biophys. J. **76,** 1101 (1999).

[61] S. M. R. Akrami, H. Nakayachi, T. Watanabe-Nakayama, H. Asakawa, and T. Fukuma, Significant improvements in stability and reproducibility of atomic-scale atomic force microscopy in liquid, Nanotechnology **25,** 455701 (2014).

[62] K. Voïtchovsky, S. A. Contera, and J. F. Ryan, Lateral coupling and cooperative dynamics in the function of the native membrane protein bacteriorhodopsin, Soft Matter **5,** 4899 (2009).

[63] L. Piantanida, H. L. Bolt, N. Rozatian, S. L. Cobb, and K. Voïtchovsky, Ions modulate stress-induced nanotexture in supported fluid lipid bilayers, Biophys. J. **113,** 426 (2017).

[64] C. Park, P. A. Fenter, K. L. Nagy, and N. C. Sturchio, Hydration and Distribution of Ions at the Mica-Water Interface, Phys. Rev. Lett. **97,** 016101 (2006).

[65] M. Ricci, P. Spijker, and K. Voïtchovsky, Water-induced correlation between single ions imaged at the solid–liquid interface, Nat. Commun. **5,** 4400 (2014).